Hydrodynamic instabilities and turbulence in pulsatile flow

Duo Xu[a,b,c,1], **Atul Varshney**[a], **Xingyu Ma**[a], **Baofang Song**[d], **Michael Riedl**[a], **Marc Avila**[b,c], and **Björn Hof**[a,1]

[a]Institute of Science and Technology Austria, Am Campus 1, Klosterneuburg 3400, Austria; [b]University of Bremen, Center of Applied Space Technology and Microgravity (ZARM), 28359 Bremen, Germany; [c]Friedrich-Alexander-Universität Erlangen-Nürnberg, Erlangen 91058, Germany; [d]Tianjin University, Center for Applied Mathematics, Tianjin 300072, China

Pulsating flows through tubular geometries are laminar provided that velocities are moderate. This in particular also applies to cardiovascular flows where inertial forces are typically too low to sustain turbulence. On the other hand flow instabilities and fluctuating shear stresses are held responsible for a variety of cardiovascular diseases. Here we report a generic instability mechanism for pulsating pipe flow that gives rise to bursts of turbulence at low flow rates. Small geometrical distortions are found to amplify the least stable mode during flow deceleration. The resulting helical vortex pattern grows rapidly, breaks down into turbulence as the flow decelerates, and eventually returns to laminar when the flow accelerates. This scenario causes shear stress fluctuations and flow reversal during each cycle, conditions that adversely affect blood vessels and promote endothelial dysfunction.

hydrodynamic instability | transition to turbulence | pulsatile flow | (non-)Newtonian fluids

Blood vessels react to hemodynamic forces and in particular the vessels inner layer, the endothelium, is highly shear sensitive. Fluctuating flow and low wall shear stress levels promote inflammation and dysfunction of the endothelium, which in turn can lead to the development of atherosclerosis lesions (1–3). However, the hydrodynamic instabilities responsible for fluctuations and varying shear stress levels are often unknown. Already for the simpler case of steadily driven flow through a straight pipe it is non-trivial to predict if the fluid motion will be smooth and laminar or highly fluctuating and turbulent. In this case the transition is 'subcritical', i.e. the laminar state is linearly stable to infinitesimal perturbations yet turbulence can arise as a result of finite amplitude perturbations provided that the Reynolds number (Re) is sufficiently large. Moreover turbulence does not appear globally but only at the location where the laminar flow is perturbed and here a localized patch, a 'puff', of turbulence is formed (4–7). Puffs travel downstream at approximately the bulk flow speed, while their size (i.e. length) remains constant. Also in pulsatile flow the transition is subcritical and again turbulence first appears in the form of puffs. Although pulsatile flows are more complex and governed by two additional control parameters, i.e. the pulsation amplitude and frequency (Womerseley number), the transition criterion commonly used is the same as that for steady pipe flow (8). For $Re < 2000$ flows are deemed laminar while above transition may occur (9). In large arteries Reynolds numbers can reach considerably larger values, however more recently it has been shown that (10, 11) for high pulsation amplitudes and low frequencies the transition to puffs is delayed. In cardiovascular flows on the other hand instabilities are commonly observed during flow deceleration. Furthermore it is unclear how geometrical deviations from the generic straight pipe geometry (like bends, unevenness and junctions) affect the flows stability.

In the following we report a hydrodynamic instability specific to pulsating flow. The instability sets in during flow deceleration, downstream of small imperfections of the pipe, such as bends or protrusions. Initially a helical wave arises which subsequently breaks down into turbulence and fluctuation levels rise before they abruptly drop during the accelerating phase where flow relaminarization sets in. This helical instability is observed at Re as low as 1000, values that are commonly reached in a variety of larger vessels. As shown the observed mechanism is generic for pulsatile flow and the helical wave corresponds to the fastest growing mode of the linearized equations.

Results

Initial experiments were carried out in a rigid straight pipe with an inner diameter of 7 mm and a total length of 12 m. The fluid was pulled through the pipe by a piston (see Fig. 1). The piston speed was sinusoidally modulated imposing a cross–sectionally averaged flow velocity $U(t) = U_m + U_o \cdot \sin(2\pi ft)$, where U_m is the mean flow speed, U_o the oscillation component of the flow speed, f the frequency and t is the time. Unless perturbed the flow remained laminar over the entire parameter range investigated. In the first set of experiments turbulent puffs were created by an impulsive injection of a small amount of fluid through a hole in the pipe wall, located $150D$ downstream of the pipe inlet. To visualize the flow structure, the water was seeded with reflective particles (fishsilver) and a light sheet was used to illuminate the mid cross section (radial-streamwise) of the pipe. An example of a puff is shown in the inset of

---

Significance Statement

The evidence of transition to turbulence in cardiovascular flow that is of close relevance to blood diseases has been repeatedly reported with inconclusive biological explanations, more unclear is the hydrodynamic origin for the unexpected transition in such low flow speeds. The hydrodynamic instability reported in this study setting in at flow rate in the range of cardiovascular flow shares important common features with the physiological evidence, accordingly it paves potentially roads towards furthering understanding of this complex problem.

www.pnas.org/cgi/doi/10.1073/pnas.XXXXXXXXXX

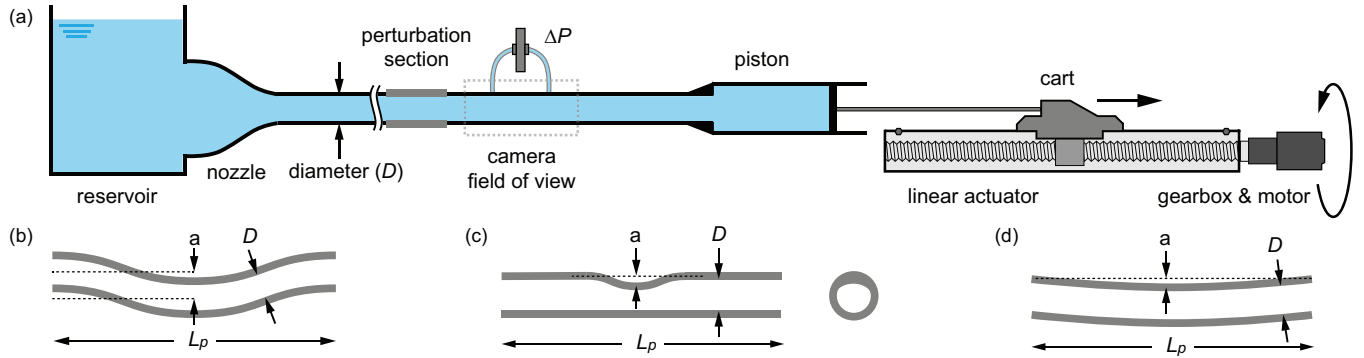PNAS | **July 7, 2019** | vol. XXX | no. XX | **1–6**

Fig. 1. (Color online) (a) Sketch of the pulsatile pipe flow setup, where the dash rectangular marks the location for camera recording and pressure drop. The flow is from left to right. Perturbation methods are sketched where D is the pipe inner diameter, L_p the length of perturbation section and a the offset: (b) cosine–shaped (stiff–bending) perturbation where $L_p = 7D$ and offset is from $0D$ (natural transition) to $0.35D$; (c) stenosis-like (unevenness) perturbation where $L_p = 5.6D$ and offset is from $0.14D$ to $0.7D$, and the right sub-panel shows the cross-section view; (c) curvature (flexi-bending) perturbation which has $L_p = 25D$ and the offset is from $0.25D$ to $1.5D$.
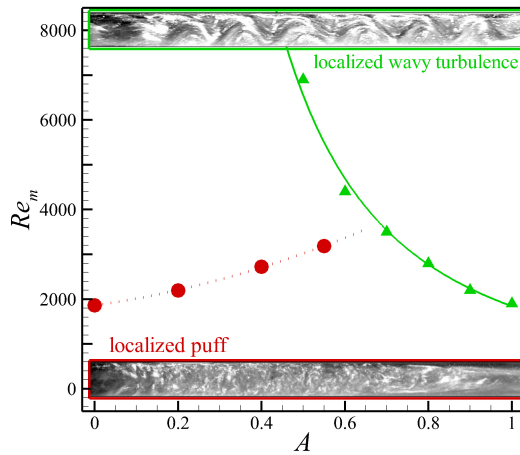

Fig. 2. (Color online) Transition Reynolds number Re_m of localized puffs (in red dotted line) and localized wavy turbulence (in green line) against the pulsation amplitude A at the same Womersley number $Wo = 5.6$. The insets show the flow visualization: the top (in green rim) shows wavy flow structures, and the bottom (in red rim) shows a puff. The flow is both from left to right.

Fig. 2 where the puff has an intense upstream interface and a gradual downstream interface, the same as in steady flow. Just like in steady pipe flow, puffs also have finite lifetimes in pulsatile flow. In order to determine the effect of the pulsation amplitude (U_o/U_m) on the puff transition we measured the puff survival rate for fixed frequency (i.e. Womersley number, $Wo = 5.6$) while the amplitude and the Reynolds number were varied. The three parameters are defined as follows $Wo = 0.5D\sqrt{2\pi f/\nu}$, $A = U_o/U_m$ and $Re_m = U_m D/\nu$, where D is the pipe diameter, ν is kinematic viscosity of the fluid. For any selected amplitude several Reynolds numbers were investigated and for each pair of parameters (A and Re_m) lifetime statistics were based on a sample of 150 puffs. Based on these data we determined the Reynolds number Re_m at the transition onset, taken as the point where 50% of the puffs survived (see ref. 10 for further details about the general methodology). In Fig. 2 we plot the dependence of Re_m on the pulsation amplitude. With increasing the amplitude the puff transition (red curve) is delayed in accordance with ref. 10.

However once the amplitude surpasses 0.7 a new instability appears and here instead of puffs a regular, wavy flow structure is observed. Also unlike puffs this structure develops at a fixed pipe location at each cycle during flow deceleration (i.e. for $0.45 \lesssim t/T \lesssim 0.75$ with dimensionless period T) and it decays during acceleration (see Movie 1 in *Supporting Information, SI*). Upon a further increase in the amplitude the instability threshold moves to smaller Re_m. The instability branch can also be continued to lower amplitudes ($A < 0.7$), in this case we did not trigger puffs by the injection mechanism and the Reynolds number was increased up to the point where the wavy instability appeared.

Inspection of the pipe revealed that the pipe segment directly upstream of the location where the wavy instability occurred, was slightly bend (with axial misalignment of approximate 500 μm). When realigning the pipe the wavy instability could be postponed to larger Re_m while further misalignment moved the instability threshold to lower Re_m. To illustrate the structural and dynamic differences between puffs and the wavy instability we compare both at the same parameter values $(Re_m, Wo, A) = (2200, 5.6, 0.85)$. In one case the pipe segment was carefully aligned and a puff was triggered using the upstream injection perturbation, in the other case no puff was injected and the flow was perturbed by the upstream bend pipe segment. Both instances are shown for the flow deceleration phase in Fig. 3: The puff begins to spread in the downstream direction, while its upstream interface remains at the same location; Over the same part of the cycle the wavy instability gradually increases in amplitude and spreads down- as well as upstream.

It should be noted that the misalignment considered above is only a fraction of a pipe diameter and in the cardiovascular context virtually all blood vessels show deviations from the idealized straight pipe case which are of that order or larger. To trigger the wavy mode in a more controlled manner we inserted a short pipe segment with a chosen moderate curvature (as sketched in Fig. 1b, see **Materials and Methods** for details), while kept the rest of pipe as straight and well aligned. A more strongly curved pipe segment the instability occurs at considerably lower Re_m (see green curves in Fig. 6) and again the transition threshold decreases with A. These findings suggest that the wavy mode, just like the instability to turbulent puffs, results from a perturbation of finite ampli-
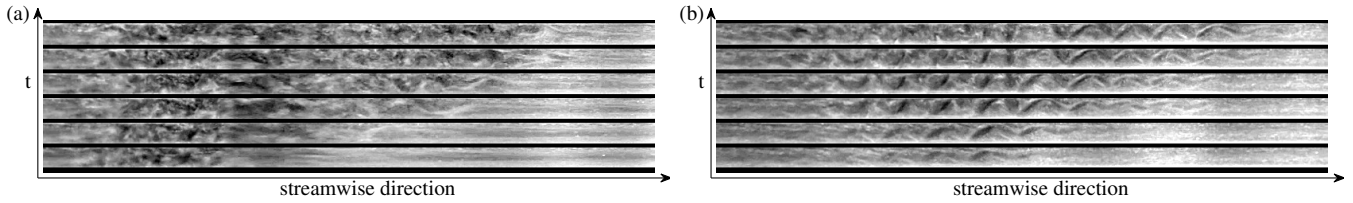
Fig. 3. Visualization of transition to turbulence in space-time diagram in pulsatile pipe flow at $(Re_m, Wo, A) = (2200, 5.6, 0.85)$: (a) Evolution of a puff with downstream interface propagating towards the downstream direction whereas the upstream interface approximately stops advection. (b) Evolution of localized helical turbulence with interfaces advecting in both downstream and upstream direction. For both panels, neighboring snapshots have an equal time interval of approximate 7 D/U_m while the pulsation period is approximately 113 D/U_m.

tude. While the puff transition is characterized by a double threshold (12), i.e. both the amplitude of the perturbation and the Reynolds numbers have to be large enough, the wavy instability has a triple threshold. Here in addition to the perturbation amplitude and the Reynolds number also the pulsation amplitude has to be sufficiently large. Moreover the type of perturbations that trigger the wavy mode appears to differ from those for puffs.

To elucidate the origins of the wavy mode we carried out numerical simulations of the Navier–Stokes equations. Albeit the laminar flow is linearly stable over the parameter range studied in the experiments, this does not exclude the possibility that modes can grow over part of the pulsation cycle, as long as they decay over the full cycle. In the simulations we tested this possibility by performing a multi-parametric optimization to determine the modes with large transient growth during a cycle. As shown in Fig. 4a initial linear perturbations can indeed considerably grow during part of the cycle and amplification factors exceed four orders in magnitude (see **Materials and Methods** for details). Enveloped by the green curve in Fig. 4a, there are sub-optimal modes which give fast energy growth in wavelength differing to the optimal mode in the wavelength of $3D$. We carried out direct numerical simulation with a sub-optimal perturbation which has the same wavelength as in the experiments. This fast growing mode corresponds to a helical mode, the same as other modes ($k \neq 0, m = 1$ for the axial and azimuthal wavenumber, respectively, see **Materials and Methods**) beneath the green line in Fig. 4a, and it resembles the experimental scenario that the instability grows from a small amplitude perturbation during the deceleration of the cycle and vanishes in the flow acceleration. To allow for efficient energy transfer among modes and to more closely approach the experimental conditions, a small amount of random noise was added to the flow field. In this case after the initial growth of the wave, indeed a break down into turbulence was found. The peak in turbulent kinetic energy is reached at $t/T \approx 0.75$, as shown in Fig. 4b, in close agreement with experiments. Again like in experiments the fluctuations rapidly decay during the acceleration phase and the flow returns to laminar (see solid line in Fig. 4b). Featured flow in the experiments, i.e. wavy structures in radial-streamwise cross section and spiral motions in radial-radial pipe cross section, can be well reproduced from the simulation, as shown in Fig. 5 (see also Movie 2 & 3 in *SI*). The transient energy growth (i.e. the black line in Fig. 4a) that takes place during flow deceleration, provides a generic mechanism that gives rise to helical vortices and a subsequent break down into turbulence.

Since the cross sections of blood vessels frequently deviate from the idealized circular case. To probe if also other geometrical factors destabilize pulsatile flow we replaced the curved segment by a straight section that includes a local constriction in form of a spherical cap (up to $D/4$ in height and a base cap diameter of $2D$, see Fig. 1c). Non–circular cross sections and constrictions are commonly found in blood vessels and may for example appear during wound healing etc. When increasing the Reynolds number at the fixed Womersley number and the pulsation amplitude, also in this case we observed helical vortices and the identical instability mechanism during the flow deceleration (see Movie 4 in *SI*). The wavy structure in this case was observed $20D$ downstream of the protrusion. At its maximum amplitude the turbulent patch stretches approximately from $15D$ to $35D$ downstream from the spherical cap.

Finally we also tested if fluid properties may influence the occurrence of the instability. While the experiments reported so far were carried out in water we next used blood as the working fluid. Blood has non-Newtonian properties and is a dense suspension of blood cells (e.g., red blood cells take up approximately 40% of the volume fraction). Experiments were carried out in a scaled down set–up with a pipe diameter of 4 mm which was otherwise followed the same working principle as the larger diameter pipe. To perturb the flow a curved section (sketched in Fig. 1d) was introduced $185D$ from the pipe inlet. Since blood is opaque and the flow structure can not be observed directly we monitored the differential pressure downstream of the curved section (see Fig. 4c). Flows were deemed unsteady if deviations in pressure were larger than 4% (i.e. over twice of the maximum standard deviation in laminar signal) when compared to the laminar pulsating flow. Like in the Newtonian flow also the pulsatile blood flow became unstable during flow deceleration and a considerable drag increase was detected approximate $20D$ downstream of the curved pipe segment. During the acceleration the flow stabilized and returned to the laminar friction value. The instability threshold for blood flow is shown by the orange symbols in Fig. 6. In this case the transition occurs at lower Re_m than for the water flows, however for the blood flow a more strongly curved segment was used to perturb the flow and we would hence expect an earlier onset. For pulsation levels typical for the Aorta i.e. $A \approx 0.94$, the Reynolds number threshold was as low as 800 and hence much lower than the commonly assumed value of 2000. Repeating the measurement under the same condition using a transparent Newtonian fluid (water), where the pressure drop and the visualization measurements were taken in the meantime for double-validation of instability identification criteria. The onset of instability (blue line in Fig. 6) and its dependence on the pulsation amplitude agrees with the other measurements. In addition, to
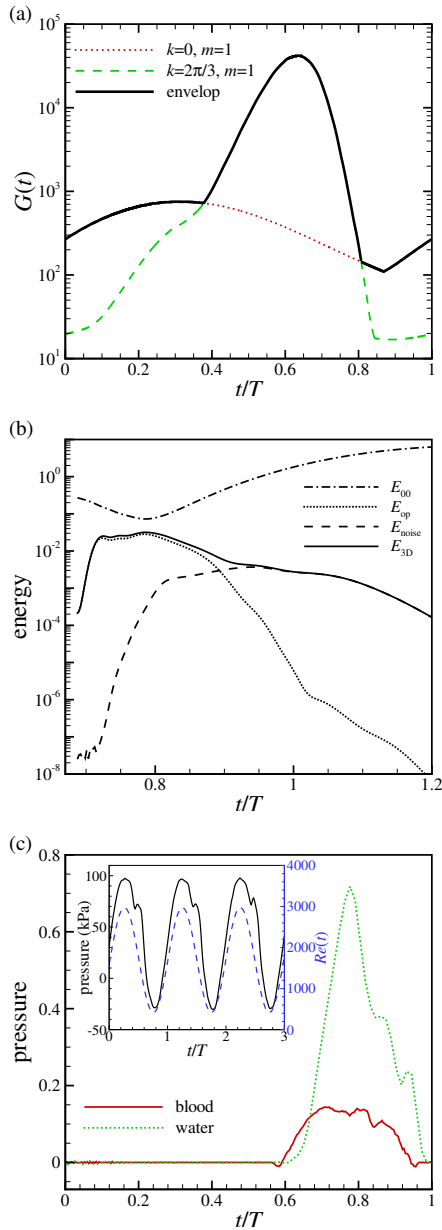
(a) legend: $k=0$, $m=1$; $k=2\pi/3$, $m=1$; envelop

y-axis: $G(t)$, x-axis: t/T

(b) legend: E_{00}, E_{op}, E_{noise}, E_{3D}

y-axis: energy, x-axis: t/T

(c) y-axis: pressure, x-axis: t/T; legend: blood, water

inset: y-axis pressure (kPa), $Re(t)$; x-axis t/T

Fig. 4. (Color online) (a) The envelop of the energy growth $G(t)$ at $(Re_m, Wo, A) = (2200, 5.6, 0.85)$ for $(k,m) = (0,1)$ (red) and $(2\pi/3, 1)$ (green) regardless of the initialized time and the duration of the perturbation. The black line shows the envelop of these two most prominent modes. (See **Materials and Methods** for details.) (b) The time series of kinetic energy for the perturbation with the noise, where E_{00} is the energy averaged axially and azimuthally, E_{op} the energy of the perturbation mode, E_{noise} the total energy except E_{00} and E_{op}, and E_{3D} the energy of three-dimensional turbulence. (c) Pressure of turbulence normalized by the laminar signal after removal of laminar flow, where the lines of blood and water flow were obtained at $(Re_m, Wo, A) = (1140, 4.0, 0.5)$ and $(1700, 5.9, 0.76)$, respectively. The measured pressure drop (black, referring left axis) and the corresponding instantaneous Reynolds number (blue, referring right axis) of the green dot line is shown in the inset.

further our study towards the cardiovascular relevance, we tested the flow of water through the visualization method in the cardiovascular flow rate as given in ref. 13. The same wavy instability was again observed during the flow deceleration followed by relaminarization as the flow was accelerated.
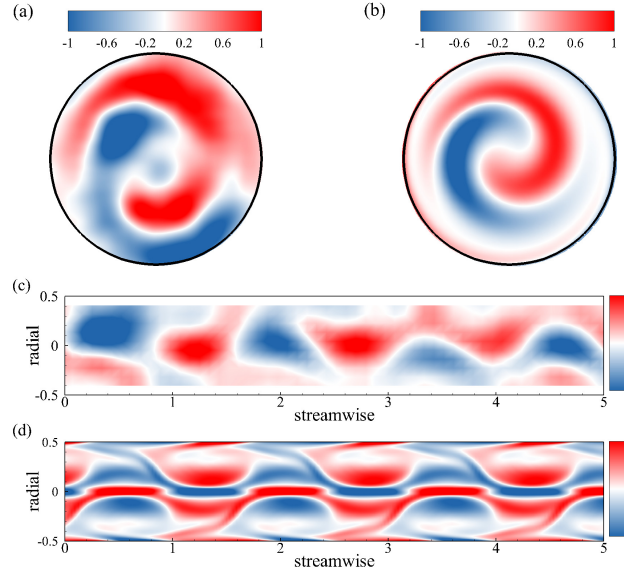

Fig. 5. (Color online) The vorticity in the cross section (radial-radial) of the pipe is contoured for experiment (a) and numerical simulation (b). In the streamwise-radial cross section the contour of the vorticity is shown for the experiment (c) and the numerical simulation (d).

Discussion and Conclusion

In summary, we report a generic instability for pulsatile pipe flow that occurs for large pulsation amplitudes and precedes the normal turbulence transition. The helical vortex mode characteristic for this instability sets in at unusually low Reynolds numbers. While finite amplitude perturbations are required to destabilize the laminar flow, weak curvature and modest pipe constrictions are sufficient. It is interesting to note that the geometrical perturbations that appear to be most efficient, are inefficient in the context of steady pipe flow. Curvature in fact has a stabilizing effect under steady conditions (14) and can even lead to relaminarization (15) at not too large Re. Constrictions on the other hand need to be very severe (16) in order to trigger puffs in steady flow. Our study hence shows that pulsatile flows are susceptible to qualitatively different and more subtle perturbations than steady pipe flows. Another unusual characteristic of the identified mechanism is that the instability only occurs during part of the pulsation cycle, i.e. the deceleration, while the acceleration relaminarizes the flow. The destabilizing property of the flow deceleration has often been observed, however to our knowledge the underlying instability mechanism has never been identified. Above findings hence suggest that pulsatile flows at large amplitudes, such as cardiovascular flows in large blood vessels, are less stable than previous studies suggested, and that at downstream of bends and constrictions, flow fluctuation levels and wall shear stresses (see *SI*) increase during part of each cycle.

Materials and Methods

Experimental Methods. Experiments were carried out in straight, rigid pipes of circular cross section: (1) a 12 m-long acrylic pipe (inner diameter $D = 7.18 \pm 0.02$ mm) gives a measurement length of
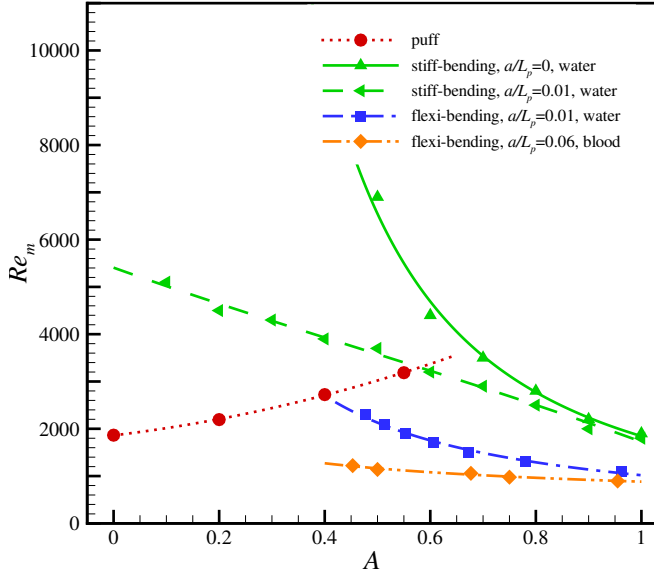
Fig. 6. (Color online) The transition Reynolds number against the pulsation amplitude for the water (Newtonian) and the blood (non-Newtonian). The transition thresholds of two perturbation methods (i.e. stiff-bending and flexi-bending) in different magnitudes are shown. Note that the data of the puff instability (red circle) and the wavy instability (green triangles) are from $Wo = 5.6$, while the data of the wavy instability (blue square) and (orange diamond) are from $Wo = 5.9$ and 4.0, respectively.

1300D for visualization and measurement of puff survival probability; (2) a glass pipe (in diameter $D = 20 \pm 0.01$ mm) was used for PIV measurement (see below); (3) another glass pipe (in diameter $D = 4 \pm 0.01$ mm) was used for experiments of non-Newtonian fluid (blood) and Newtonian fluid (water). This excludes the origin of turbulence with pipe properties, e.g. diameter tolerance, materials and etc. Pipe segments are joined by Perspex connectors for seamless fits. The pipe segments are positioned and carefully aligned on a long aluminum profile. The pipe is connected through a trumpet shaped convergence section to a reservoir (see the nozzle in Fig. 1a). The rear end of the pipe is connected to a piston system driven by a motor through a gearbox. The speed of the motor is precisely controlled by a PC with a National Instrumentation card. This produces the cross–section averaged flow speed $U(t) = U_m + U_o \cdot \sin(2\pi f \cdot t)$. For the entire parameter regime under investigation the pipe flow is laminar unless employing perturbations. The temperature of the fluid was measured before the experiments for accurate kinematic viscosity of the fluid and so as the Reynolds number. For non-Newtonian fluid, unit milliliter of fresh pig blood was stabilized with 40 units anticoagulant agent (Sigma-Aldrich). The kinematic viscosity of the blood (at laboratory room temperature 20°C) was measured to be $\nu = 8 \pm 2$ mm^2/s.

In experiments of the puffs, to ensure generating a single localized puff, a tiny volume of fluid was injected in volume flow rate approximate 2% of the pipe flow through a 1 mm hole in the pipe wall, which was 150D downstream from the nozzle for sufficient pipe entry length. The duration of the injection was adjusted through an electronically controlled valve to cover the same phase for experimental runs. A light sheet was used to illuminate the mid-plane (radial-streamwise) of the pipe. The fluid was seeded with fishsilver flakes for flow visualization. A digital camera (MatrixVision BlueFox 121G) was placed at about 1300D downstream from the injection point to record whether puffs decayed or survived. In each individual run, only one puff was generated in the pipe. The 150 runs for a fixed Reynolds number and a fixed pulsation amplitude at $Wo = 5.6$ give approximately the converged survival probability of the puffs.

In experiments of wavy/helical instability, three perturbations methods as sketched in Fig. 1(b–d) were used, the first two of which were produced through a three-dimensional printer. The ends of the perturbation section was further finished in a milling machine for smooth connecting with the pipe segments. The 'stiff-bending' perturbation (see Fig. 1b) preserves the cosinusoidal shape, the inner diameter of which at the cross section is D the same as the pipe. This perturbation mimics the non-straight nature of vessels. The 'stenosis-like' perturbation (see Fig. 1c) is straight except that a protrusion in form of a spherical cap that the base has a diameter of $2D$ and the height ranges from 0 to $D/4$. This perturbation mimics the physiological condition that the diameters of vessels are not perfectly constant and that practical vessel constriction exists. The third perturbation segment ('flexi-bending') is composed of a semi-flexible tube that has the same inner diameter as the pipe. The ends of the tube and of the pipe segments were specially finished to minimize the unsmoothness of the connection. The perturbation level, i.e. the axis offset, was produced accurately by the gauge screw. This perturbation looses constrains of shape preserved and partially considers the flexibility nature of blood vessels. In the same configuration of visualization in the puff experiments, a Phantom high-speed camera (in resolution of 2400×1800 pixels^2) was placed at approximate 20D downstream of the perturbation section to record the flow, at sampling rates up to 30 frames per second. At the same position, the pressure drop of the instability across 40D streamwise distance at a sampling rate of 50 Hz was measured through a high-sensitivity differential pressure sensor (HSC series, Honeywell).

To obtain the spatial velocity field of the wavy instability, particle image velocimetry (PIV) measurements were carried out in the glass pipe with the diameter of $D = 20$ mm. Here the perturbation of shape-preserved stiff-bending or the spherical cap protrusion, as sketched in Fig. 1(b,c), were used. Two-dimensional planar PIV measurements were carried out in the mid cross section (radial-streamwise) of the pipe, while stereo-PIV measurements were carried out in the cross section (radial-radial) to provide three-component velocity fields. The measurements were performed at approximate 20D downstream from the perturbation section, the field-of-view of which approximately centered at the streamwise origin of the wavy instability. The fluid (i.e. water) was seeded homogeneously with hollow-glass spheres which have diameters of approximate 10 μm. The laser sheet in thickness of approximate 1 mm was formed from a continuous wave laser (center wavelength of 532 nm, FC 532N-5W) through a group of lenses to illuminate the field-of-view. A prism was used to minimize the imaging distortion from the curvature of the pipe wall. The Phantom camera was used to capture tracer images with the frame rates optimized for fulfilling the requirements of time intervals in PIV. Commercial software DaVis (LaVision) was used to retrieve the velocity vectors through a multi-step algorithm, and 32×32 pixels^2 in window size with 50% overlap was set for the final step for both sets of the PIV measurements.

Numerical Methods. We considered an incompressible Newtonian fluid driven through a circular straight pipe at a pulsatile flow rate. The lengths and velocities are normalized also with the pipe diameter D and the mean velocity U_m, and consequently the time is rendered dimensionless with the advection time unit D/U_m and the non-dimensional pulsation period is $T = \pi Re_m/(2Wo^2)$. The instantaneous Reynolds number reads $Re(t) = Re_m \cdot [1 + A \cdot \sin(2\pi t/T)]$, while the mean Reynolds number is also $Re_m = U_m D/\nu$ with kinematic viscosity of the fluid ν.

For linear stability analysis, considering the time-dependence of the base flow, we employed the adjoint-based method (17) to calculate the optimal growth for our system. According to ref. 17, the *linearized* Navier–Stokes equations read

$$\frac{\partial \boldsymbol{u}'}{\partial t} + \boldsymbol{u}' \cdot \boldsymbol{\nabla} \boldsymbol{U}_b + \boldsymbol{U}_b \cdot \boldsymbol{\nabla} \boldsymbol{u}' = -\boldsymbol{\nabla} p' + \frac{1}{Re_m} \boldsymbol{\nabla}^2 \boldsymbol{u}', \ \boldsymbol{\nabla} \cdot \boldsymbol{u}' = 0 \ \ [1]$$

and the adjoint system reads

$$\frac{\partial \boldsymbol{u}^*}{\partial t} - \boldsymbol{u}^* \cdot (\boldsymbol{\nabla} \boldsymbol{U}_b)^{\mathrm{Tr}} + \boldsymbol{U}_b \cdot \boldsymbol{\nabla} \boldsymbol{u}^* = \boldsymbol{\nabla} p^* - \frac{1}{Re_m} \boldsymbol{\nabla}^2 \boldsymbol{u}^*, \ \boldsymbol{\nabla} \cdot \boldsymbol{u}^* = 0. \ \ [2]$$

Here $\boldsymbol{u}'$ is the tiny velocity fluctuation with respect to the base flow $\boldsymbol{U}_b(t)$, p' the pressure fluctuation, the starred quantities are the adjoints of the primed variables and Tr denotes matrix transpose.

No-slip boundary condition is imposed for both $\boldsymbol{u}'$ and $\boldsymbol{u}^*$. The maximum possible growth of the kinetic energy at time τ, $E(\tau)$, of an initial perturbation $\boldsymbol{u}'(0)$ given at $\boldsymbol{U}_b(0)$, i.e.,

$$G(0,\tau) = \max_{\|\boldsymbol{u}'(0)\|_2 \neq 0} \frac{E(\tau)}{E(0)}, \qquad [3]$$

can be calculated as the maximum eigenvalue of the operator $A^*(\tau)A(\tau)$, where $A(\tau)$ and $A(\tau)^*$ are the action operators to map $\boldsymbol{u}'(0)$ to $\boldsymbol{u}'(\tau)$ according to Eq. 1 and $\boldsymbol{u}^*(0)$ to $\boldsymbol{u}^*(\tau)$ according to Eq. 2, respectively. Operationally, this method integrates Eq. 1 forward from $t = 0$ to $t = \tau$ and Eq. 2 backward from $t = \tau$ to $t = 0$. Subsequently, the Krylov subspace method is used to approximate the maximum eigenvalue of $A^*(\tau)A(\tau)$. This operation is iterated until the eigenvalue is sufficiently converged. In our problem, the base flow $\boldsymbol{U}_b(t)$ is analytically given in ref. 18. We solved the linearized equations using Chebyshev-Fourier-Fourier spectral method, in which velocity and pressure are represented as

$$B(r,\theta,z,t)_{(k,m)} = \hat{B}_{(k,m)}(r,t)e^{i(kz+m\theta)} + \text{cc.,} \qquad [4]$$

where k (real number) and m (integer) are the axial and azimuthal wave numbers, respectively, $\hat{B}_{(k,m)}$ is the Fourier coefficient of the mode (k,m) and cc. represents the complex conjugate. The integration in time was performed using a second-order-accurate Adams-Bashforth/backward differentiation scheme and the incompressibility condition is imposed using the projection method (19). We used a time-step size $\Delta t = 0.025$ and 96 Chebyshev-Guass-Labatto grid points in the radial direction. The entire analysis was performed using Matlab with adapting scripts from ref. 20.

A multi-parameter optimization process was carried out through the adjoint analysis. The obtained optimal modes, i.e., the eigenvectors associated with the maximum eigenvectors, set reasonable candidates for the perturbations for the direct numerical simulations to numerically reproduce the wavy instability scenario. The analysis considers combinations of the axial mode $k \in [0, 2\pi/3]$, the azimuthal mode $m \in [0, 2]$, the initial perturbation time $(t - \tau)/T \in [0, 1]$ and the duration $\tau/T \in [0, 1]$. Initial perturbation $\boldsymbol{u}'(t - \tau)$ was initialized at time $t - \tau$ and the maximum energy growth $G(t - \tau, \tau)$ (see Eq. 3) was explored at time t using the method described in the previous section. For each paired (k, m), the enveloped energy growth $G(t)$ was obtained over all $t - \tau$ and τ. The optimal mode $(k, m) = (0, 1)$ as in the ordinary steady pipe flow gives peaked $G(t) \approx 800$ at $t/T = 0.25$ in the pulsatile pipe flow (see red dotted

line in Fig. 4c). $(k \neq 0, m = 1)$ modes start to dominate from $t/T \approx 0.4$, which is enveloped by the mode $(k, m) = (2\pi/3, 1)$ that gives the largest $G(t)$ of approximate 4×10^4 (green dash line). The overall envelop of the examoled two modes as depicted by the black solid line in Fig. 4c shows that large energy growth dominates in the deceleration phase in a pulsation period.

Accordingly, we carried out direct numerical simulations of the Navier–Stokes equations in cylindrical coordinates (r, θ, z) through the 'openpipeflow' code (21), where the *linear* and *non-linear* terms are fully considered. The code uses primitive variables and a pressure Poisson equation formulation with an influence-matrix technique. In the radial direction, spatial finite-difference discretization is employed with nine-point stencils, and points are densely clustered close to the pipe wall for capturing of small flow structures. No-slip boundary conditions are applied at the pipe wall. Spectral methods are employed along the pipe axis (z) and azimuthal (θ) direction to present periodicity, and the variables are expanded in Fourier modes

$$V(r,\theta,z) = \sum_{k=-K}^{K} \sum_{m=-M}^{M} \hat{V}_{(k,m)}(r)e^{i(\alpha kz + m\theta)} \qquad [5]$$

where $\hat{V}_{k,m}$ is the complex Fourier coefficient of the mode (k, m), k and m are the wavenumbers of the modes along the axial and azimuthal directions, respectively, and $L_z = 2\pi/\alpha$ gives the pipe length. The simulations were carried out at $(Re_m, Wo, A) = (2200, 5.6, 0.85)$ with ± 196 and ± 96 Fourier models along axial and azimuthal direction and 96 radial points in an approximate $12D$ pipe. The Fourier modes (except the perturbed modes) were initialized with small values for energy transfer among modes in fast Fourier transforms operations in the code (see dash line in Fig. 4b), and it imitated the background noise in the experimental setup.

1. Nerem RM, Cornhill JF (1980) The role of fluid mechanics in atherogenesis. *J. Biomech. Eng* 102:181.
2. Cunningham KS, Gotlieb AI (2005) The role of shear stress in the pathogenesis of atherosclerosis. *Lab. Invest* 85:9–23.
3. Gimbrone MA, García-Cardeña G (2016) Endothelial Cell Dysfunction and the Pathobiology of Atherosclerosis. *Circ. Res* 118:620–636.
4. Wygnanski I, Champagne F (1973) On transition in a pipe. part 1. the origin of puffs and slugs and the flow in a turbulent slug. *Journal of Fluid Mech.* 59:281–335.
5. Hof B, Westerweel J, Schneider TM, Eckhardt B (2006) Finite lifetime of turbulence in shear flows. *Nature* 443:59.
6. Hof B, de Lozar A, Kuik DJ, Westerweel J (2008) Repeller or attractor? selecting the dynamical model for the onset of turbulence in pipe flow. *Phys. Rev. Lett.* 101:214501.
7. Avila M, Willis AP, Hof B (2010) On the transient nature of localized pipe flow turbulence. *J. Fluid Mech.* 646:127–136.
8. Davis SH (1976) The Stability of Time-Periodic Flows. *Annu. Rev. Fluid Mech* 8:57–74.
9. Avila K, et al. (2011) The onset of turbulence in pipe flow. *Science* 333:192–196.
10. Xu D, Warnecke S, Song B, Ma X, Hof B (2017) Transition to turbulence in pulsating pipe flow. *J. Fluid Mech.* 831:418–432.
11. Xu D, Avila M (2018) The effect of pulsation frequency on transition in pulsatile pipe flow. *J. Fluid Mech.* 857:937–951.
12. Grossmann S (2000) The onset of shear flow turbulence. *Rev. Mod. Phys.* 72:603–618.
13. Fraser KH, Meagher S, Blake JR, Easson WJ, Hoskins PR (2008) Characterization of an abdominal aortic velocity waveform in patients with abdominal aortic aneurysm. *Ultrasound in Med. & Biol.* 34:73–80.
14. Kühnen J, Braunshier P, Schwegel M, Kuhlmann HC, Hof B (2015) Subcritical versus super-

15. Sreenivasan KR, Strykowski PJ (1983) Stabilization effects in flow through helically coiled pipes. *Exp. Fluids* 1:31–36.
16. Durst F, Loy T (1985) Investigations of laminar flow in a pipe with sudden contraction of cross sectional area. *Computers & Fluids* 13:15–36.
17. Barkley D, Blackburn HM, Sherwin SJ (2008) Direct optimal growth analysis for timesteppers. *Int. J. Numer. Meth. Fluids* 57:1435–1458.
18. Womersley JR (1955) Method for the calculation of velocity, rate of flow and viscous drag in arteries when the pressure gradient in known. *J. Physiol.* 127:553–563.
19. Hugues S, Randriamampianina A (1998) An improved projection scheme applied to pseudospectral methods for the incompressible Navier–Stokes equations. *Int. J. Numer. Meth. Fluids* 28:501–521.
20. Trefethen LN (2000) *Spectral Methods in MATLAB*. (SIAM, Philadelphia).
21. Willis AP (2017) The Openpipeflow Navier–Stokes solver. *SoftwareX* 6:124–127.
22. Hahn C, Schwartz MA (2009) Mechanotransduction in vascular physiology and atherogenesis. *Nat. Rev. Mol. Cell Biol.* 10:53–62.
23. Meng H, Tutino VM, Xiang J, Siddiqui A (2014) High wss or low wss? complex interactions of hemodynamics with intracranial aneurysm initiation, growth, and rupture: Toward a unifying hypothesis. *American Journal of Neuroradiology* 35:1254–1262.
24. Ku DN, Giddens DP, Zarins CK, Glagov S (1985) Pulsatile flow and atherosclerosis in the human carotid bifurcation. positive correlation between plaque location and low oscillating shear stress. *Arterioscler. Thromb. Vasc. Biol.* 5:293–302.
25. Glagov S, Zarins C, Giddens DP, Ku DN (1988) Hemodynamics and atherosclerosis. insights and perspectives gained from studies of human arteries. *Arch. Pathol. Lab. Med.* 112:1018–1031.

critical transition to turbulence in curved pipes. *J. Fluid Mech.* 770:R3.